WILEY-VCH

DOI: 10.1002/ (please add manuscript number)
Article type: Full Paper

3D-Printed Hygroscopic Matrices Based on Granular Hydrogels for Atmospheric Water Adsorption and On-Demand Defogging

Xiaochun Wu, *Suxu Wang*, *Jun Zhao*, *Jingjing Li*, *Yuke Sun*, *Zhihang Wang**, *Petri Murto*, *Hongzhi Cui** & *Xiaofeng Xu**

X. Wu, S. Wang, J. Zhao, J. Li, Y. Sun

Prof. X. Xu, email: xuxiaofeng@ouc.edu.cn

Prof. H. Cui, email: cuihongzhi@ouc.edu.cn

College of Materials Science and Engineering, Ocean University of China, Qingdao 266100, China.

Dr. Z. Wang, email: z.wang@derby.ac.uk

School of Engineering, College of Science and Engineering, University of Derby, Markeaton Street, Derby DE22 3AW, United Kingdom.

Department of Materials Science and Metallurgy, University of Cambridge, Cambridge CB3 0FS, United Kingdom.

Dr. P. Murto

Department of Chemistry and Materials Science, Aalto University, Kemistintie 1, 02150 Espoo, Finland.

Keywords: Atmospheric water adsorption, granular hydrogels, hygroscopic polymers, 3D matrices, water vapor adsorption

ABSTRACT

Sorption-based atmospheric water harvesting is an emerging technology with great potential in clean water production, humidity management and passive cooling applications. Hygroscopic salt-embedded composites as porous aerogels and hydrogels represent intriguing 3D porous sorbents across a broad humidity range. However, none of the commonly used hygroscopic materials — including inorganic powders, organic polymers, and inorganic–organic hybrids — are inherently printable, limiting kinetics-enhancing strategies and application-specific use. Herein, hygroscopic 3D matrices are developed based on granular hydrogel-mediated direct-ink writing (DIW). Microgels cross-linked with percolating polymer networks synergistically improve printability and shape fidelity of the inks, enabling precise printing of previously unprintable hygroscopic composites. Hygroscopic 3D matrices with well-defined hierarchical porosity — spanning millimeter-scale lattice channels, micrometer-scale wrinkled surfaces, and nanometer-scale granular hydrogel assemblies — maximize surface areas and mass transporting pathways, enhancing sorption/desorption kinetics, structural durability and performance stability. Compared to hygroscopic aerogels, the hygroscopic matrix reduces raw material requirement by 53% and increases specific surface areas by 5.8-fold, leading to a 1.4-fold improvement in water uptake (2.85 g g^{-1}). This work significantly broadens the applicability and versatility of hygroscopic materials through a microgel-mediated DIW approach, and shines light on 3D-printable hygroscopic matrices tailored for reliable and user-defined dehumidification and anti-fogging.

1. Introduction

Atmospheric water vapor constitutes a vast, yet frequently underutilized reservoir of freshwater. This volume (~12,900 trillion liters) is nearly six times greater than that of the world's surface water.[1] Unlike conventional water sources, atmospheric moisture is geographically ubiquitous and largely independent of local hydrological conditions.[2] In this context, atmospheric water vapor presents a dual role: it serves both as a valuable resource and a potential environmental hazard. Atmospheric water harvesting (AWH) stands out as a promising strategy for decentralized clean water production and agricultural irrigation, reducing reliance on large-scale water transport infrastructure and associated operational costs.[3] Conversely, elevated humidity levels also present significant challenges, including material corrosion, postharvest food spoilage, increased risks of foodborne illnesses and exacerbation of heat-related health issues.[4] As a result, a wide range of anti-fogging, cooling and dehumidification technologies has been developed to manage temperature and humidity across industrial settings, buildings, electronics, logistics and personal environments.[5]

The contents and physical states of atmospheric water are critical factors in AWH applications and humidity management.[6] In unsaturated air (relative humidity, RH < 100%), water primarily exists in the vapor phase, accounting for ~98% of atmospheric water. On the other hand, saturated air (100% RH) contains small liquid droplets, which represent only ~2% of atmospheric water. Traditional AWH techniques — such as fog harvesting and dew collection — rely on the presence of mist or high ambient humidity levels (typically > 60% RH). As a result, these AWH methods face significant geographical, climatic and energy constraints, limiting their applicability in diverse environments. As an emerging strategy, sorption-based AWH stands out as the only approach effective across a broad RH range (10 − 100% RH).[7] Sorption-based AWH technologies employ hygroscopic materials to capture water vapor from ambient air through physical adsorption and chemical interactions.[8] The absorbed moisture

can be released via desorption, typically activated by low-grade heat sources such as solar energy, electronic waste heat, or even body temperature.[9] Leveraging reversible moisture sorption/desorption cycles, sorption-derived AWH technologies provide environmentally friendly and adaptable solutions for clean water production, irrigation, dehumidification, passive cooling and protective packaging — unconstrained by conventional limitations of temperature, humidity and energy input.[10-11] As a result, the development of advanced hygroscopic materials, system-level devices, customized and hybrid AWH applications has become a topic of growing interest.[12-14]

Widely used inorganic desiccants (i.e., silica gel and zeolite) are limited by low water uptake capacities and high dehydration temperatures, making them energy-ineffective under repeated sorption−desorption cycles.[15] Although inorganic hygroscopic salts (i.e., LiCl, LiBr and $CaCl_2$) feature superior moisture sorption capacities, they suffer from uncontrolled deliquescence, flow and recrystallization during cycling. These issues result in inconsistent water uptake, deteriorated kinetics, salt leakage and corrosion, thereby compromising their long-term reliability. Conventional organic sorbents (i.e., glycerin) are typically in liquid form, posing challenges for geometric stabilization. While emerging inorganic/organic hybrid sorbents (i.e., metal−organic complexes or metal−organic frameworks) exhibit enhanced high sorption/desorption kinetics, their powder form still significantly limits processability and practical integration.[16-17]

To overcome these inherent limitations, hygroscopic components are increasingly integrated into polymer matrices to engineer next-generation composite sorbents, since polymers provide superior processability and tunable physicochemical properties.[18] Their sorption properties are jointly governed by both chemical nature of hygroscopic components and hierarchical morphologies of polymeric matrices.[19] The sorption capacity and enthalpy of these composites are mainly determined by the types and concentrations of the primary hygroscopic

components.[20] Hydrophilic or hygroscopic matrices can be fabricated from either natural biopolymers (i.e., polysaccharides) or synthetic polymers (i.e., polyelectrolytes).[21] Towards different applications, tailored 2D and 3D architectures (i.e., fabrics, aerogels, hydrogels and foams) provide enhanced structural versatility, tunable pore characteristics and performance-enhancing strategies.[22] These porous structures significantly increase reactive surface areas and facilitate vapor diffusion. The nano-, micro- and macropores enable efficient salt solution retention through capillary action, enhancing moisture sorption−desorption kinetics.[23] The salt-in effect induced by polyelectrolytes, large-volume swelling of hydrophilic networks and thermos-responsive hydrogels synergistically increase hygroscopic salt contents, salt solution sorption and water release.[24]

From a fabrication-method perspective, hygroscopic 2D fabrics are predominantly fabricated via electrospinning and wet-spinning techniques.[25-26] For 3D porous matrices, template-assisted approaches (i.e., sol−gel transition, freeze drying, ambient drying and foaming) represent the state-of-the-art fabrication methods.[27] However, conventional hygroscopic aerogels, hydrogels and foams frequently lack precise control over pore architecture, limiting their ability to achieve tunable structural scales, customizable functionalities and application-specific performance. In response, the rational design and controlled fabrication of hygroscopic salt-embedded polymer composites with precisely tailored multiscale porosity has emerged as a cutting-edge frontier, while expanding their application potential.[28-38]

3D printing enables unprecedented design flexibility through mold-free fabrication and broad compatibility with composite materials.[39] Recent advances in 3D printing techniques (i.e., direct-ink writing and vat photopolymerization) have emerged as powerful tools for rapid prototyping and achieving unparalleled local control over 3D geometry and pore topology in photothermal, hygroscopic or hydrophilic 3D matrices.[39-43] Their capabilities overcome the major limitations of hygroscopic aerogels, hydrogels and foams, which lack the speed,

adaptability and resolution required to accurately reproduce and modulate complex pore morphologies and spatial distributions.[44-48] Despite notable progress, the full potential of 3D printing hygroscopic materials remains constrained by the stringent rheological requirements of precursor inks. For instance, in direct-ink writing (DIW), ideal inks should possess in proper viscosity, shear-thinning behavior, rapid curing and self-supporting properties to ensure smooth extrusion, precise deposition and high structural fidelity.[49] None of the commonly used hygroscopic materials — including inorganic powders, organic polymers, and inorganic–organic hybrids — are inherently printable or compatible with direct printing techniques. Rheology modifiers such as cellulose nanofibers (CNFs), nanoclay, Pluronic F-127 or carbomer are typically incorporated to improve printability.[50] However, these additives, while water-soluble, have negligible moisture sorption capacity and thereby reducing the overall water uptake per unit weight of the resulting composites. Moreover, the incorporation of hygroscopic salts often disrupts the electrostatic interactions within ionic polymers, promoting aggregation and impairing ink fluidity. As a result, the formulation of printable inks composed entirely of hygroscopic materials remains challenging. Direct printing of hygroscopic polymers (i.e., polysaccharides and polyelectrolytes) without non-hygroscopic additives represents a promising route, potentially enabling future fabrication of hygroscopic salt-embedded polymer composites. Nevertheless, none of the hygroscopic polymers investigated thus far exhibit adequate printability.[51]

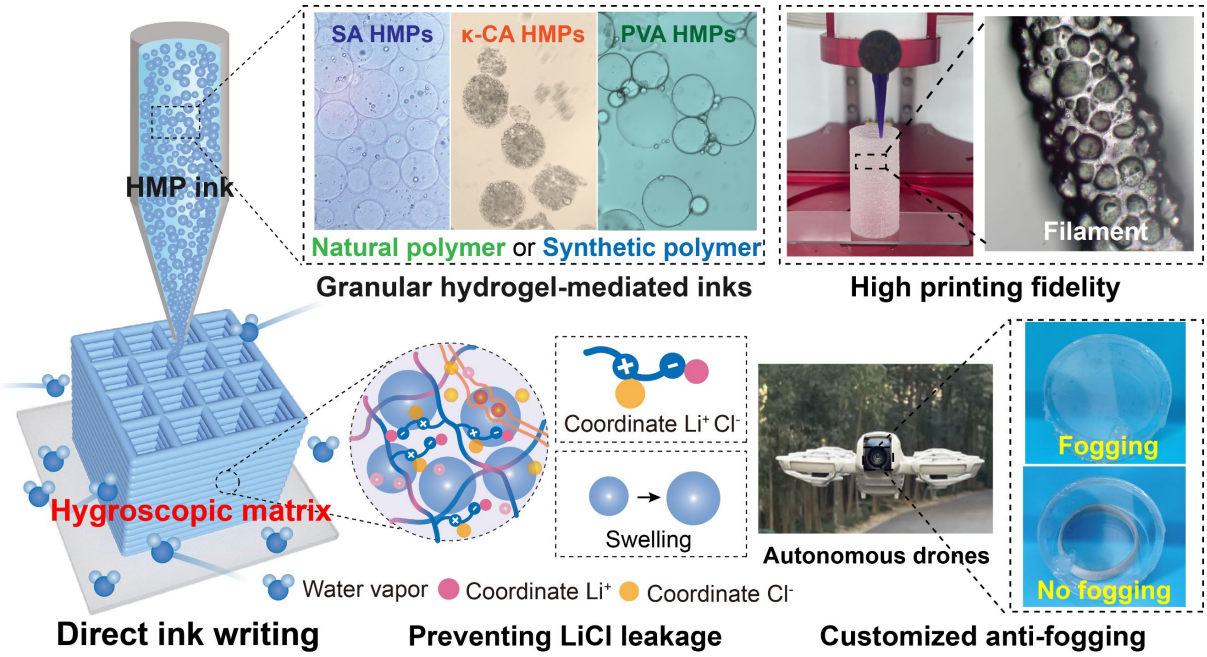

Figure 1. Schematic illustration and digital photographs of granular hydrogels, cross-linking networks, 3D-printed hygroscopic matrices and customized anti-fogging applications.

In this contribution, hygroscopic 3D matrices with well-defined hierarchical structures were fabricated via DIW using a group of granular hydrogel-based inks (**Figure 1**). The inks, composed of hygroscopic inorganic–organic components and cross-linked networks within granular hydrogels (microgels), were systematically optimized in terms of viscosity, rheology and modulus, synergistically improving the printability, printing fidelity, self-supporting properties and applicability. Embedding LiCl within jammed microgels enhanced moisture uptake. Zwitterionic copolymer-mediated percolating networks provided mechanical reinforcement and large-volume swelling, ensuring structural integrity and minimizing LiCl leakage. 3D-printed lattice structures with hierarchical porosity maximized surface areas and mass transporting pathways, enhancing sorption/desorption kinetics and performance stability during cyclic operation. As key outcomes of this study, the optimized hygroscopic matrix reduced raw material requirement by 53% and increased specific surface areas by 5.8-fold, leading to 1.4-fold higher water uptake (2.85 g g^{-1} at 90% RH over 48 h) compared to the conventional hygroscopic aerogel. The water uptake capability ranks it among the top-

performing 3D-printed hygroscopic materials reported to date. This microgel-mediated DIW strategy not only broadens the hygroscopic material scope for 3D printing but also enables on-demand fabrication of diverse hygroscopic geometries (e.g., cubic and cylindrical forms) tailored for application-specific dehumidification and anti-fogging. These hygroscopic 3D matrices offer significant advantages over traditional hygroscopic materials in terms of structural versatility, processability and customized applications.

2. Results and discussion

2.1 Fabrication, characterization and optimization of granular hydrogels and inks

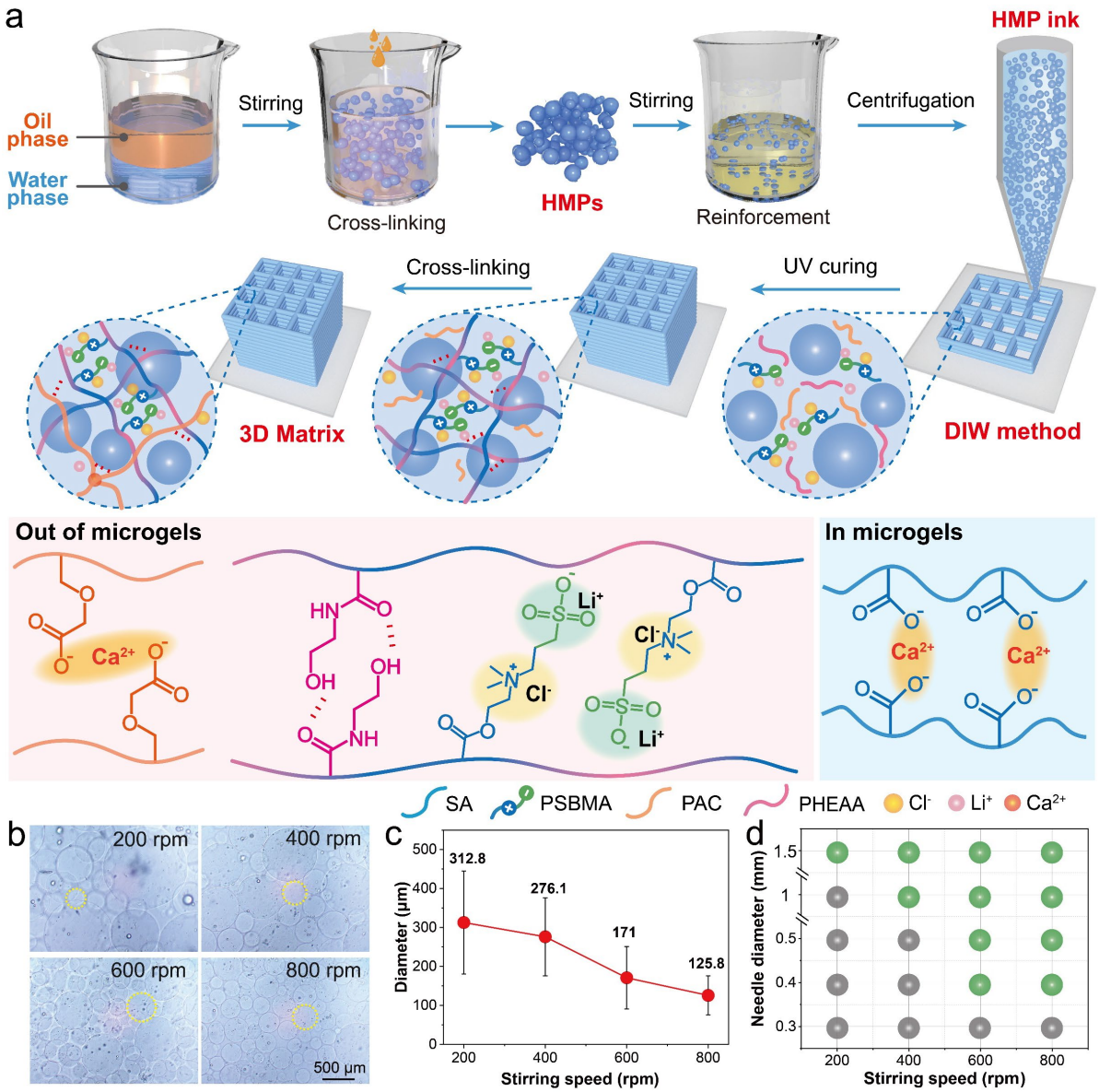

Figure 2. (a) Flowchart of the fabrication of SA-HMPs, HMP inks and related structural components and cross-linking reactions. (b) Optical microscope images and (c) diameter distribution of SA-HMPs formed at different rotational speeds. (d) Printability characterization of SA-HMP inks (gray dots represent non-printable while green dots represent printable).

Sodium alginate (SA), a naturally derived polyanionic polymer, consists of two monomeric units: β-D-mannuronic acid (M) and α-L-guluronic acid (G), interconnected via 1→4 glycosidic bonds. The abundant carboxyl groups and sodium ions in the repeating M and G residues impart inherent hygroscopicity and water-retention capacity to SA.[52] Neat SA powder exhibits an equilibrium water uptake of ~0.35 g g^{-1} under 90% RH (Figure S1, Supporting Information). However, the aqueous SA solution behaves as Newtonian fluids with inherently low viscosity, rendering it unsuitable for 3D printing. The sol−gel method remains the conventional approach for fabricating SA-derived aerogels and hydrogels. Hence, SA-based hydrogels are inherently difficult to print without chemical modification or the incorporation of rheological additives. To address this limitation, the rheological requirements of DIW can be inherently satisfied when precursor inks are formulated as jammed microparticles.[53] Jammed microparticles are immobilized via dense packing and physical interactions, resulting in a solid-like behavior. When stress exceeding the yield point is applied, the structure yields and undergoes significant plastic deformation, leading to a fluid-like state. Importantly, when the applied stress is reduced below the yield threshold or removed entirely, the gel rapidly re-establishes its internal structure, reverting to the original jammed state.[54] This microgel strategy significantly broadens the material range suitable for 3D printing.[55] As a result, our study introduces a modified microgel-based inks incorporating percolating networks to enable 3D printability of SA-based hygroscopic hydrogels.

The fabrication of SA-based microgels, cross-linking reactions and printable inks are illustrated in **Figure 2a**. Initially, neat SA and surfactants were dissolved in water and mixed with paraffin

oil to form a biphasic solution. Vigorous vortexing of this mixture induced emulsification, generating water−in−oil droplets. Subsequent dropwise addition of a $CaCl_2$ solution to the emulsion initiated the cross-linking of SA microparticles through coordination bonds between Ca^{2+} ions and carboxyl groups, preferentially within the G-block regions, leading to the formation of stable hydrogel microparticles (HMPs). The resulting SA-HMPs were thoroughly washed with petroleum ether, ethanol and deionized (DI) water to remove residual oil and surfactants. The suspension was centrifuged to yield jammed HMPs amenable to DIW processing. The sizes of HMPs can be precisely controlled by modulating the stirring speed during emulsification (**Figure 2b**). Increasing the stirring speed from 200 to 800 rpm gradually reduced the average diameter of HMPs from 312.8 to 125.8 μm (**Figure 2c** and Figure S2, Supporting Information). To evaluate extrudability, HMPs were tested with various needle diameters (**Figure 2d**). The extrusion pressure was gradually increased until consistent, uniform filaments were achieved. Under a proper printing pressure of 8 psi, HMPs prepared at 800 rpm min^{-1} exhibited superior extrudability across a broad nozzle size range (0.4 − 1.5 mm), highlighting the crucial influence of HMP sizes on printability.

Although SA-HMPs facilitated the DIW fabrication of a free-standing 3D structure, its mechanical strength under external stress remained limited by weak interparticle interactions, primarily governed by Van der Waals forces (Figure S3, Supporting Information). To reinforce SA-HMPs and enable load-bearing 3D structures, additional percolating networks capable of post-printing cross-linking were incorporated with SA-HMPs, inspired by a stone-cottage printing strategy.[56] Specifically, the ink formulation comprised SA-HMPs dispersed in an aqueous solution containing: [2-(methacryloyloxy)ethyl]dimethyl-(3-sulfopropyl) ammonium hydroxide (DMAPS), *N*-hydroxyethylacrylamide (HEAA), polyanionic cellulose (PAC), lithium chloride (LiCl), cross-linker and photoinitiator. Following 12 h of immersion, the mixture was centrifuged to obtain jammed SA-HMP inks suitable for DIW processing.

The DMAPS monomer's zwitterionic structure, featuring equimolar anionic and cationic groups, exhibited a "salt-in" effect (anti-polyelectrolyte effect) with LiCl. This zwitterionic network effectively coordinated Li^+ and Cl^- ions, minimizing LiCl leakage.[57] However, neat PDMAPS hydrogels displayed inherent brittleness. To address this, HEAA was incorporated as a comonomer, leveraging its multiple hydrogen bond donor/acceptor sites to enhance mechanical properties of the printed matrix. Copolymer (denoted as P(PDMAPS-*co*-HEAA)) based hydrogels were synthesized with a total monomer concentration fixed at 30 wt%. Preliminary compressive and tensile tests were conducted to evaluate the mechanical properties. Incorporating 10 wt% HEAA increased the compressive strength by 3.5-fold, while 20 wt% HEAA boosted the compressive strength by 5.7-fold at 30% compressive strain (Figure S4a, Supporting Information). This copolymerization strategy also synergistically improved tensile strength, elongation at break and toughness (Figure S4b, Supporting Information). A minimal PAC addition (0.5 wt%) served as a rheological modifier, increasing the apparent viscosity of the ink from 9.4 to 22.1 mPa·s, and enabling smooth extrusion of uniform filaments at low printing pressure (8 psi) (Figure S5, Supporting Information). Following printing, the DMAPS and HEAA monomers were polymerized via UV-initiated free-radical polymerization to form P(PDMAPS-*co*-HEAA), while subsequent Ca^{2+} ions cross-linked the PAC backbones. These sequential processes created percolating polymer networks featuring multiple covalent and ionic bonding within and out of HMPs (Figure 2a). The incorporation of percolating polymer networks (i.e., P(PDMAPS-*co*-HEAA) and PAC) enhanced the structural robustness of the printed matrix, compared to those fabricated with neat SA-HMP ink (Figure S3, Supporting Information).

To study the influence of hygroscopic salts on ink performance, LiCl concentrations in SA-HMP inks were systematically varied from 0.05 to 0.4 g mL^{-1}. HMP inks made from 0.05 and 0.1 g mL^{-1} LiCl solutions exhibited well-defined microgels and formed continuous filaments,

indicating excellent extrudability (Figure S6 and S7, Supporting Information). Increasing LiCl concentrations slightly increased the minimum extrusion pressure from ~3.1 psi to ~3.4 psi. However, higher LiCl concentrations (> 0.2 g mL^{-1}) induced excessive osmotic-driven shrinkage of HMPs, resulting in the formation of HMP aggregates that disrupted filament continuity. Furthermore, hygroscopic properties of printed SA-HMP filaments with varying LiCl concentrations were characterized under 90% RH and at 25 °C (Figure S8, Supporting Information). All filaments exhibited spontaneous water vapor sorption, with both kinetics and equilibrium capacity scaling with the LiCl concentrations. However, the image sequence reveals notable LiCl solution leakage from printed filaments over time when the HMP inks contained elevated LiCl concentrations (> 0.2 g mL^{-1}) (Figure S9, Supporting Information). Taking into account the extrudability, hygroscopicity and LiCl retention, we optimized the SA-HMP ink formulation using a 0.1 g mL^{-1} LiCl. Notably, the printed SA-HMP filament based on this ink composition achieved water uptake of 3.10 g g^{-1} after 48 h while ensuring excellent printability and negligible LiCl leakage. To ensure consistency, all HMP inks were prepared using the same LiCl concentration (0.1 g mL^{-1}), thereby maintaining a consistent LiCl-to-polymer ratio within printed matrices. Energy-dispersive X-ray spectroscopy (EDS) mapping confirmed homogeneous distribution of C, O, N, S, Cl and Ca throughout the printed filaments, indicating uniform component distribution, formation of interpenetrating networks and successful incorporation of designed cross-linking reactions (Figure S10, Supporting Information).

2.2 Rheology, printability and mechanical characterization

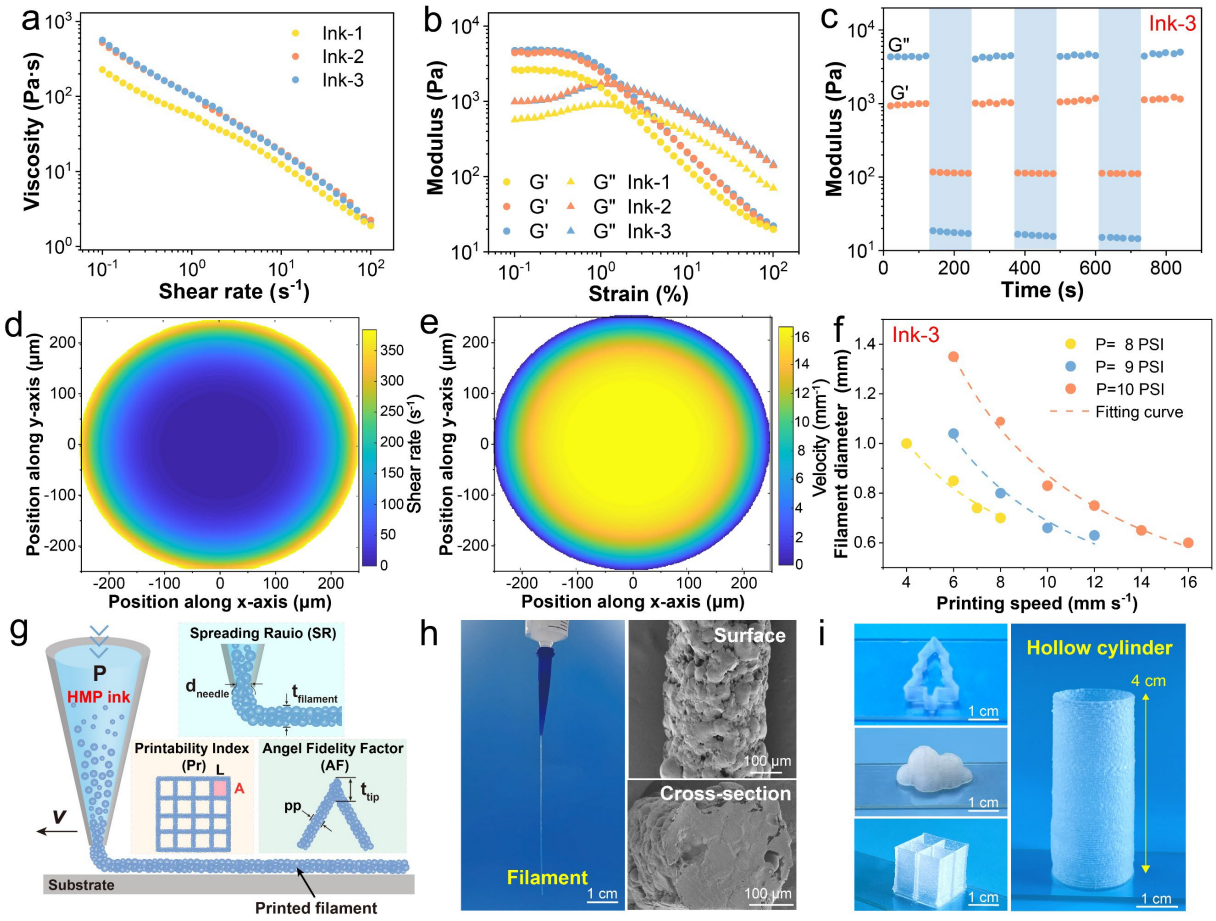

Figure 3. Rheological properties of different inks: (a) shear viscosities under shear rate sweep, (b) G′ and G″ under amplitude sweep and (c) Shear recovery measurement under alternate low (1%) and high (100%) stains at a constant frequency of 1 Hz. Rheological simulation of Ink-3 based on Herschel-Bulkley fluid model: (d) shear rate and (e) flow velocity distribution within a nozzle. (f) Printability optimization of printing pressure and speed. (g) Schematic illustration of main printing parameters used for evaluating printing precision. (h) Morphological characterization of printed filaments and (i) 3D-printed complex structures based on HMP inks.

The rheological properties of SA-HMP inks, critical for printability and dimensional accuracy, were modulated by varying centrifugation speeds (5000, 6000 and 7000 rpm) to control microgel jamming densities, yielding three HMP ink formulations (denoted as Ink-1, Ink-2 and Ink-3). Optical microscopy reveals that as centrifugation speed increased, small microgels progressively filled the interstitial spaces among larger microgels (Figure S11, Supporting

Information). To quantify the degree of HMP jamming, microscopy images were analyzed using Image J. The projected microsphere area per unit area was measured as 88%, 91%, and 99% for Ink-1, Ink-2, and Ink-3, respectively. Correspondingly, the total solid contents—determined using a halogen moisture analyzer—were 29.1%, 31.2%, and 32.8% for Ink-1, Ink-2, and Ink-3, respectively. These results confirm that both the jamming degree and polymer contents of SA-HMPs increased with the centrifugation speed, which contributed to improving the inks' shear-thinning behavior and self-supporting capability. As the degree of jamming increased, the minimal extrusion pressure also rose from 2.5 psi for Ink-1 to 3.4 psi for Ink-3, due to denser particle packing that enhanced the inherent resistance to shear flow.

Higher centrifugation speeds also increased the zero-shear viscosities from 227.5 to 563.5 Pa s of these HMP inks due to enhanced particle packing and interactions. The shear viscosity profiles of HMP inks as a function of shear rate are presented in **Figure 3a**. All inks exhibited a significant decrease in shear viscosity as shear rate increased from 10^{-1} s^{-1} to 100 s^{-1}, indicating shear-thinning behavior, which can be expressed by the constitutive equation of the Herschel-Bulkley model, as expressed by equation 1,[58]

$$\tau = \tau_0 + m(\gamma)^n \qquad (1)$$

where τ and τ_0 represent the apparent and yield strengths, respectively, γ is the shear rate, m is the consistency index, n is the power-law exponent. A Newtonian fluid exhibits n = 1, while n > 1 and n < 1 correspond to shear-thickening and shear-thinning behavior, respectively. Fitting the data revealed pronounced shear-thinning properties for these HMP inks, with n = 0.29 (Ink-1), 0.24 (Ink-2) and 0.22 (Ink-3) (Figures S12, Supporting Information). On the other hand, the neat SA solution (5 wt%) displayed a low shear viscosity of ~2.0 Pa s, with no shear-thinning behavior observed over the shear rate range from 10^{-1} s^{-1} to 100 s^{-1} (Figure S13, Supporting Information). The absence of shear thinning in neat SA solution limited its printability. These

results highlight the critical role of microgel-based rheological modification in enabling 3D printing of otherwise unprintable materials.[59] Increasing the LiCl concentrations from 0 to 0.3 g mL^{-1} LiCl increased the shear-thinning behavior of the inks, which can be attributed to osmotic shrinkage of HMPs at higher salt concentrations (Figure S14, Supporting Information). This shrinkage led to tighter microgel packing and increased resistance to shear flow.

The storage modulus (G′) and loss modulus (G″) of HMP inks under oscillatory strain sweep are plotted in **Figure 3b**. All inks exhibited viscoelastic behavior under low strain (below 1.8%), as evidenced by G′ exceeding G″. Notably, Ink-3 exhibited the highest G′ and G″ values, indicating its superior elasticity (resisting deformation) and enhanced energy dissipation capacity (viscous response), respectively. The crossover point (G′ = G″) for Ink-3 occurred at a critical stress of 1600 Pa and strain of 1.8% — well within the operational range of DIW processing. Beyond this point, a sharp decrease in G′ relative to G″ signified a transition to dominant viscous flow, a key requirement for DIW processing. In addition, the dynamic shear recovery behavior of HMP inks was systematically investigated by applying varying oscillatory strains across multiple cycles. Both G′ and G″ values of all inks exhibited remarkable reversibility, transitioning between a solid-like elastic state (G′ > G″ at 0.1% strain) and liquid-like viscous state (G″ > G′ at 100% strain) through multiple cycles (**Figure 3c**, Figure S15, Supporting Information). The negligible decay in moduli and sub-second recovery times demonstrates robust network resilience within the inks. This rapid, fully reversible gel−fluid transition enables precise extrusion and immediate shape retention — another key requirement for maintaining high shape fidelity. Building upon its superior rheological properties, Ink-3 was selected as the ideal ink for subsequent printing and characterization.

Numerical simulations employing the Herschel-Bulkley model investigated critical flow dynamics (shear rate and flow velocity distributions) of SA-HMP inks within a nozzle during printing (volumetric flow rate: 0.146 mL min^{-1}, printing speed: 10 mm s^{-1}, nozzle diameter:

0.5 mm) (Figure S16, Supporting Information). With increasing jamming from Ink-1 to Ink-3, the central plug region expanded, while the shear zone near the nozzle wall progressively narrowed. This trend agrees well their rheological properties, since denser jamming resulted in higher viscosity, thereby increasing resistance to shear deformation. Moreover, the velocity rate profiles represent steeper velocity gradients within the reduced shear zones to maintain a constant volumetric flow rate across Ink-1 to Ink-3. For Ink-3, The shear rate distribution presents pronounced shear rate heterogeneity, ranging from 370 s^{-1} at the nozzle wall to zero at the center, exhibiting characteristic plug flow behavior (**Figure 3d**). High shear rates overcame the yield stress threshold at the nozzle wall, while preserving a viscoelastic, deformation-resistant core. On the other hand, the velocity profile exhibited an inverse relationship to the shear rate distribution, with near-zero flow velocity at the nozzle wall due to viscoelastic resistance, transitioning to maximum velocity in the plug flow region (**Figure 3e**). Moreover, both shear rates and plug flow dimensions exhibited strong dependence on extrusion parameters. Notably, increasing the extrusion rates from 0.05 to 0.3 mL min^{-1} through a 0.5 mm nozzle elevated the wall shear rate (130 − 785 s^{-1}), while simultaneously reducing the plug flow radius from 125 to 100 μm. The preserved structural integrity of the plug flow region within the nozzle can minimize extrusion deformation, thereby enhancing printing fidelity printed by Ink-3.

Systematic evaluation of printing parameters revealed critical pressure−speed−diameter relationships for Ink-3 (**Figure 3f**). Excessively high or low printing speeds led to non-printable conditions. At a constant print speed, increasing air pressure resulted in larger filament diameters, whereas at a fixed print pressure, higher printing speeds reduced filament diameters. Notably, the 10-psi condition offered exceptional process latitude with stable printing across 6 − 16 mm s^{-1} speeds and 1.35 − 0.60 mm diameters, providing wider operational window compared to 8 and 9 psi. The parameter space (printing pressure: 10 psi and printing speeds: 10 mm s^{-1}) was selected for its balanced combination of resolution, throughput and fidelity,

establishing quantitative guidelines for scalable Ink-3 printing.

Following the printing process using Ink-3, printing accuracy was quantitatively assessed using three main metrics: spreading ratio (SR), angle fidelity factor (AF) and printability index (Pr). These parameters were evaluated using both individual filaments and interconnected grids. These main parameters used for printing accuracy evaluation is illustrated in **Figure 3g**. SR is quantified as the ratio of deposited filament width to nozzle diameter, as expressed by equation 2,[60]

$$\mathrm{SR} = \frac{t_{\mathrm{filament}}}{d_{\mathrm{nozzle}}} \qquad (2)$$

where t_{filament} represents the width of extruded strand, and d_{nozzle} is the diameter of the printing nozzle. SR directly reflects ink coalescence behavior, where SR ≈ 1 indicates ideal filament definition with minimal spreading. For Ink-3, SR was measured at 1.2, exhibiting small deviation from the intended filament width.

To quantify geometric fidelity in printing angular shapes, an angle fidelity factor (AF) was introduced. AF is defined as the ratio of filament thickness at angular junctions (60°, 90° and 120°) to linear segments, as expressed by equation 3,[60]

$$\mathrm{AF} = \frac{t_{\mathrm{tip}}}{\mathrm{pp}} \qquad (3)$$

where t_{tip} and pp represent the thickness at the tip and along the filament, respectively. For Ink-3, AF values were measured to be 1.2 (60°), 1.15 (90°) and 1.02 (120°), exhibiting a clear angular dependence. The elevated AF values at acute angles (60 − 90°) indicate strand overlapping and material accumulation at angular junctions during printing. On the other hand, the near-unity AF at 120° approached ideal geometric fidelity. Notably, the SR and AF (90°) values of Ink-3 fall within the range of those reported for representative microgel inks in the

literature, as summarized in Figure S17, Supporting Information.

To evaluate shape retention based on grid structures, Pr factor was introduced. Pr is defined as the ratio of preserved sharpness at pore corners in a grid, as expressed by equation 4,[60]

$$\mathrm{Pr} = \frac{\pi}{4C} = \frac{L^2}{16A} \qquad (4)$$

where L represents the perimeter and A is the enclosed area. Generally, Pr = 1 indicates ideal square pores, Pr < 1 reflects rounded pores due to filament merging/flow and Pr > 1 represents irregular extrusion with excessive material accumulation.[60] For Ink-3, Pr was measured at 0.96 and this near-unity value demonstrates its exceptional self-supporting behavior. Two printable inks containing different LiCl concentrations (0.05 and 0.1 g mL^{-1}) exhibited comparable printing resolution, as evidenced by similar spreading ratio (SR = 1.23 and 1.20), angle fidelity factor at 90° (AF = 1.21 and 1.15) and printability index (Pr = 0.92 and 0.96), respectively.

Based on the optimized printing conditions, continuous filaments with diameters matching the nozzle's inner dimension were achieved (**Figure 3h**). Scanning electron microscope (SEM) characterization reveals a micro-structured surface morphology, featuring uniformly distributed microparticles while maintaining filament integrity. As a result, Ink-3 was able to print intricate 3D structures such as trees, clouds and matrices, exhibiting high shape fidelity and dimensional stability (**Figure 3i** and Supporting Video S1). The sinking degree (r) was used to quantitatively evaluate the self-standing property of the inks through freeform fabrication of hollow cylinders, as expressed by equation 5,[61]

$$r = \frac{H}{H_0} \qquad (5)$$

where H and H_0 represent the actual and designed heights of a hollow cylinder. Ink-3 achieved an 80-layer structure (height = 4 cm) with near-ideal stability (r = 1). On the other hand, the hollow cylinders printed by Ink-1 and Ink-2 collapsed after printing 16 and 36 layers,

respectively, leading to low *r* values of 0.2 and 0.45 (Figure S18, Supporting Information).

Mechanical properties of 3D-printed structures using Ink-3 were evaluated through uniaxial tension and compression tests. Rectangular strips (10 × 50 mm^2) subjected to uniaxial tension exhibited anisotropic behavior, with filaments perpendicular to the tensile direction showing lower Young's modulus, tensile strength, fracture strain, and toughness compared to parallel filaments (Figure S19, Supporting Information). In addition, cyclic compression tests on printed solid cubes (15 × 15 × 10 mm^3) under 30% strain revealed minimal stress degradation (< 7.3% loss) and plastic deformation (< 7.6%) over 100 loading/unloading cycles. The overlapping hysteresis loops from the stress−strain curves demonstrate exceptional deformation resistance and rapid recovery (Figure S20, Supporting Information). The measured compressive stress values fall within the range reported for microgel-based materials fabricated via DIW processing.[62-63] Although higher LiCl concentrations enhanced compressive stress, the inks with LiCl content above 0.1 g mL^{-1} exhibited poor printability (Figure S21, Supporting Information). These results highlight the durability and fatigue resistance of the printed hygroscopic materials based on optimized SA-HMP ink.

2.3 Water sorption and desorption characterization

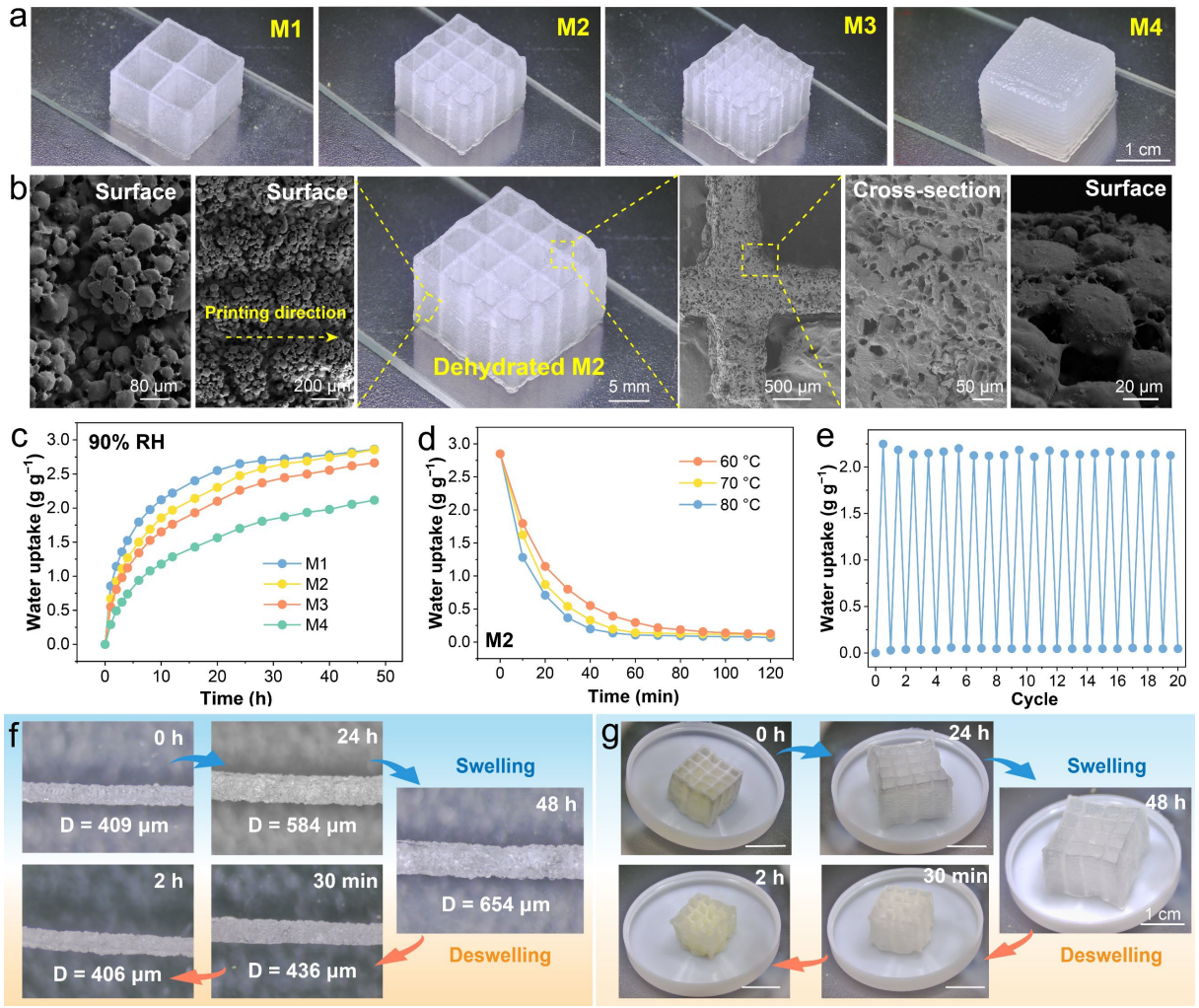

Figure 4. (a) Digital photographs of 3D-printed matrices. (b) Morphological characterization of freeze-dried M2. (c) Water vapor sorption characterization under 90% RH. (d) Water desorption characterization of M2 at varying temperatures. (e) Water uptake and release characterization in 20 moisture sorption−desorption cycles. Digital photographs of (f) 2D filaments and (g) 3D matrix (M2) during a sorption−desorption cycle.

Four hygroscopic 3D matrices with varying lattice structures were printed based on Ink-3 (**Figure 4a**). Maintaining identical dimensions (15 × 15 × 10 mm^3), three matrices with 2×2, 4×4, and 6×6 cuboid frameworks were designated as M1, M2, and M3, respectively. A fully dense hydrogel (denoted as M4) was printed with 100% infill and characterized as a control group. M4 required 0.93 g cm^{-3} of Ink-3 for printing. In contrast, the fabrication of 3D matrices markedly reduced ink consumption. The ink requirement decreased with increasing cuboid

dimensions, from 0.58 g cm^{-3} for M3, 0.44 g cm^{-3} for M2, to 0.22 g cm^{-3} for M1. Surface area-to-mass ratio, referring to the external surface area of each 3D matrix, was calculated. Compared to M4, the 3D-printed matrices also exhibited significantly higher surface-area-to-mass ratios (specific surface areas), which increased from 97.5 cm^2 g^{-1} for M3 to 129.5 cm^2 g^{-1} for M1 (Figure S22, Supporting Information). These results highlight one of the main advantages of 3D printing: the ability to enhance interfacial surface areas for water sorption/desorption, while reducing material consumption.

The morphologies of freeze-dried aerogel matrix (M2) were further characterized (**Figure 4b**). Macroscopic imaging revealed a well-defined millimeter-scale lattice structure, exhibiting high printing fidelity and structural retention following lyophilization. SEM images depict distinct multiscale features within M2: the side surfaces exhibited pronounced wrinkling, with well-aligned filaments oriented along the printing direction. The truss-like lattice walls were composed of stacked layers of these printed filaments, while each filament consisted of densely jammed HMPs. This hierarchical porosity — spanning millimeter-scale lattice channels, micrometer-scale wrinkled surfaces, and nanometer-scale HMP assemblies — provides rich interfaces and diffusion pathways for water vapor sorption/desorption.

Water vapor sorption performance of M1−M4 was evaluated at 25 °C under 90% RH, with all samples pre-dehydrated via lyophilization to ensure consistency. The changes of water uptake over time are plotted in **Figure 4c**. M1, M2 and M3 exhibited water uptake of 2.86, 2.85 and 2.66 g g^{-1} after 48 h, respectively, significantly surpassing M4 (2.11 g g^{-1}). This enhanced performance of M1−M3 stemmed from their hierarchical pore structures, which integrates: 3D lattice channels for vapor diffusion, 2D wrinkled surfaces and 1D HMP arrays for water molecular sorption, synergistically maximizing moisture diffusion and vapor−material interactions. Hygroscopic SA-HMPs further facilitated efficient water retention and diffusion. Among M1−M3, the total hygroscopic material content within the matrices also influenced

water uptake, with M1 exhibiting the highest capacity due to its superior specific surface area, which maximized moisture-accessible interfaces per unit mass compared to M2 and M3. However, M1's minimized cuboid framework (2×2) exhibited structural instability during moisture sorption/desorption cycles. On the other hand, M2 optimally balanced hygroscopicity and mechanical robustness, making M2 ideal for further study. Under varying RH levels from 50 to 90% RH, M2 afforded water uptake of 0.38, 0.62, 1.09, and 2.85 g g^{-1}, respectively, indicating a broad adaptability in dynamic humidity environments (Figure S23, Supporting Information).

Raman spectroscopy was employed to elucidate the state of absorbed water molecules in M2 during water vapor sorption. The water molecules within the hydrogel matrix are classified into three distinct states based on their interaction with polymer chains.[64] Bound water forms stable hydrogen bonds with the polymer network and remains non-freezable below 0 °C due to its highly ordered structure. Free water behaves similarly to bulk water, showing minimal interaction with the polymer and exhibiting conventional freezing behavior. Intermediate water, by contrast, forms weaker hydrogen bonds that facilitate the formation of metastable clusters, requiring less energy to evaporate than free water.[65] The presence of intermediate water plays a pivotal role in governing hydrogel dehydration kinetics, as these weakly-bound clusters require lower activation energy for release compared to both bound and free water states.[66] Raman spectroscopic analysis of M2 during vapor sorption revealed a characteristic −O−H stretching band centered at 3400 cm^{-1}, whose intensity scaled with the hydration level of M2 (Figure S24a, Supporting Information). Spectral deconvolution resolved four distinct sub-peaks. Peaks at 3232 and 3408 cm^{-1} corresponded to free water, characterized by the formation of tetrahedrally coordinated hydrogen bonding. Peaks at 3515 and 3624 cm^{-1} represented intermediate water, featuring disrupted/weak hydrogen bonds that enable low-energy evaporation. The free-to-intermediate water ratio (FW/IW) increased from 2.5 to 3.8 during

sorption, exhibiting a progressive transition toward bulk water at saturation (Figure S24b, S24c and S24d, Supporting Information).

Water desorption experiments of M1−M4 were conducted under identical dehydration conditions. All pre-dried matrices were first placed into a 90% RH chamber for 48 h. Subsequently, the samples were transferred to a hot-air oven and heated at 80 °C to induce water release. M1 and M2 exhibited rapid water desorption kinetics, releasing 98.0% and 97.6% of the absorbed water within 2 h (Figure S25, Supporting Information). On the other hand, M3 released 77.3% of absorbed water, while M4 showed the lowest water release kinetics within the same period. Additional tests on M2 under controlled dehydration temperatures (60 − 80 °C) showed 95.5%, 96.0% and 97.6% water release within 2 h, respectively (**Figure 4d**). This near-complete water desorption, achieved through direct hot-air activation, highlights M2's low-energy dehydration pathways — a critical advantage for cyclic operation.

Cyclic sorption−desorption testing was conducted to evaluate the long-term stability of M2, with each cycle comprising 22 h vapor sorption at 25 °C/90% RH and subsequent 2 h thermal desorption at 80 °C. Remarkably, M2 maintained exceptional stability over 20 cycles, preserving an average sorption capacity of 2.15 g g^{-1} with no detectable performance degradation. SEM analysis confirmed the absence of LiCl aggregation on the matrix surface over these cycles (Figure S26, Supporting Information). EDS mapping reveals a uniform distribution of Cl throughout M2, with no signs of concentration variation or anisotropic enrichment. These result reveal that the percolating networks of ionic polymers effectively prevented salt leakage through a "salting-in" mechanism. Specifically, zwitterionic DMAPS units provided electrostatic stabilization via their quaternary ammonium and sulfonate groups. In addition, ionic PAC chains contributed additional coordination sites through carboxylate groups, forming stable Li^+−carboxylate complexes that prevented LiCl phase separation. This synergistic immobilization effect indicates one of the main advantages of incorporating ionic

polymers as the percolating networks with HMPs for preventing LiCl leakage from the hygroscopic matrices.

The water vapor sorption process in LiCl-embedded polymer composites progresses through three distinct stages: (i) chemisorption, (ii) deliquescence and (iii) salt solution absorption.[18] While stages (i) and (ii) are governed by LiCl contents, stage (iii) is facilitated by the matrix's hierarchical porosity (enabling capillary forces) and controlled swelling (ensuring salt solution retention). The swelling and deswelling properties of both 2D filament and 3D matrix during hydration-dehydration cycles were characterized through time-resolved imaging. Quantitative analysis revealed a 1.6-fold diameter increase in Ink-3 printed filaments after 48 h under 90% RH, with complete dimensional recovery after 2 h desorption at 80°C (**Figure 4f**). Moreover, M2 exhibited no structural collapse during repeated water vapor sorption−desorption cycles (**Figure 4g**). This cyclic stability primarily stemmed from the elastic polymer networks and hierarchical reinforcement imparted by aligned filaments formed via DIW processing. By molecularly dispersing and stabilizing LiCl within this porous, swellable, and mechanically robust scaffold, the resulting LiCl-embedded polymer matrix (M2) achieved sustained hygroscopicity, minimal salt leakage, and excellent structural and performance stability.

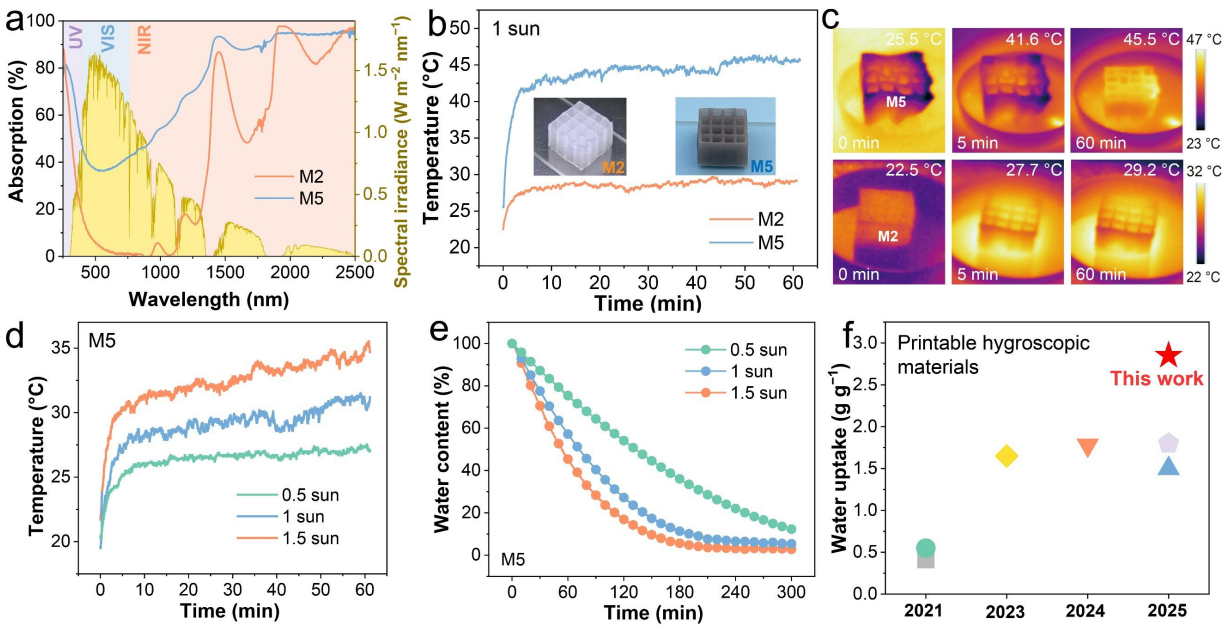

Figure 5. (a) Absorbance spectra of M2 and M5. (b) Surface temperatures and (c) IR images of M2 and M5 under 1 sun over time. (d) Surface temperatures and (e) solar-driven water desorption under varying solar intensity over time. (f) Summary of water uptake capability of 3D-printable hygroscopic materials.

The absorptance spectrum of printed filament layers within M2 was characterized using UV−Vis−NIR spectroscopy (**Figure 5a**). These thin, semitransparent layers displayed a near-white appearance with minimal absorbance across the visible spectrum (Vis, 480 − 780 nm). On the other hand, a gradual increase in absorbance was observed in the near-infrared range (NIR, 780 − 2500 nm). Despite this NIR absorption enhancement, the overall sunlight absorption remained significantly lower than that of conventional photothermal materials, suggesting limited photothermal conversion efficiency. To harness the largely untapped spectrum of solar irradiation, this study integrated supplementary photothermal components into Ink-3, leading a photothermal and hygroscopic ink (denoted as Ink-4). Specifically, a small amount (0.5 wt%) of antimony-doped tin oxide (ATO) nanoparticles was incorporated within Ink-4, transforming M2 into a photothermally active matrix (designated as M5). ATO nanoparticles exhibit unique spectrum-selective optical properties, combining high visible-light transmittance and near-infrared absorptance, driven by their intrinsic localized surface plasmon resonance (LSPR) effects.[67] These characteristics have enabled their widespread application as: (i) photothermal conversion components in smart textiles,[26] and (ii) transparent heat barriers in energy-efficient glazing systems.[68] When incorporated into M5, the ATO nanoparticles induced a dramatic enhancement in broadband solar absorption, increasing absorptance in both visible and NIR wavelength ranges compared to pristine M2. Compared to Ink-3, the incorporation of ATO nanoparticles in Ink-4 enhanced the shear-thinning behavior, due to the jamming effect of microparticles that improved the rheological properties (Figure S27, Supporting Information). Mechanically, the presence of ATO nanoparticles retained the compressive strength of the printed structures under 30% strain (Figure S28, Supporting

Information). Regarding printing resolution, Ink-4 exhibited comparable SR (1.15), AF at 90° (1.08) and Pr (0.97), relative to Ink-3.

SEM characterization reveals that the M5 surfaces retained the jammed HMP arrays observed in M2, with a comparable filament dimension (Figure S29, Supporting Information). In addition, EDS elemental mapping depicts uniform distribution of Sn and Sb signals throughout M5. The homogeneous dispersion of other elements (C, O, N, S, Cl and Ca) confirms successful integration of photothermal components without disrupting the original structural framework of M2. Moreover, M5 exhibited water uptake of 2.60 g g^{-1} after 48 h under 90% RH, indicating 91% retention of M2's moisture sorption capability (2.85 g g^{-1}) (Figure S30, Supporting Information). These results indicate that incorporating a small amount of ATO nanoparticles only marginally affected the hygroscopic performance while adding photothermal functionality. In contrast, conventional photothermal materials (i.e., nano-carbon powder and carbon nanotubes) required significantly higher loadings (2.0 wt%), which markedly compromised printability and significantly diminished the moisture sorption capacity of the hygroscopic 3D matrix.

Under 1 sun, pre-dried M5 (15 × 15 × 10 mm^3) exhibited significantly enhanced photothermal performance compared to M2. Infrared thermography revealed that M5 reached a maximum surface temperature of 45.5 °C over 1 h, representing a 55.8% increase (ΔT = 16.3 °C) over M2's peak temperature (**Figure 5b** and **5c**). This result demonstrates the effective photothermal conversion enabled by ATO incorporation while maintaining the structural integrity of the matrix upon heating. Furthermore, the photothermal dehydration performance of water-saturated M5 was evaluated under varying solar intensities (AM 0.5 − 1.5 sun). Within 1 h of irradiation, the M5 surface exhibited rapid temperature increases by 8.4 °C (0.5 sun), 13.3 °C (1 sun) and 19.3 °C (1.5 sun), exhibiting intensity-dependent heating behavior (**Figure 5d**). This photothermal response directly correlated with enhanced water release rates, where M5

achieved over ~94% water removal under 1 sun (**Figure 5e**). At the highest intensity (1.5 sun), near-complete dehydration (~98%) occurred within 3 h, highlighting the high solar-driven desorption efficiency of M5.

A performance benchmark of state-of-the-art 3D-printed hygroscopic materials is summarized in **Figure 5f** and Table S1, Supporting Information. Among them, M2 delivered high water uptake of 2.85 g g^{-1} under 90% RH and retained < 4.3% capacity variance over 20 sorption−desorption cycles, placing it among the top-performing 3D-printed hygroscopic systems reported to date. Notably, its 3D lattice structure with hierarchical porosity reduced raw material requirement by 53% and enhanced water uptake by 1.4-fold compared to the bulk hygroscopic aerogel (M4). This result highlights the cost-effectiveness of 3D-printed hygroscopic matrices, which require significantly less material while outperforming conventional hygroscopic composites in moisture sorption and water desorption.

2.4 Customized dehumidification and anti-fogging applications

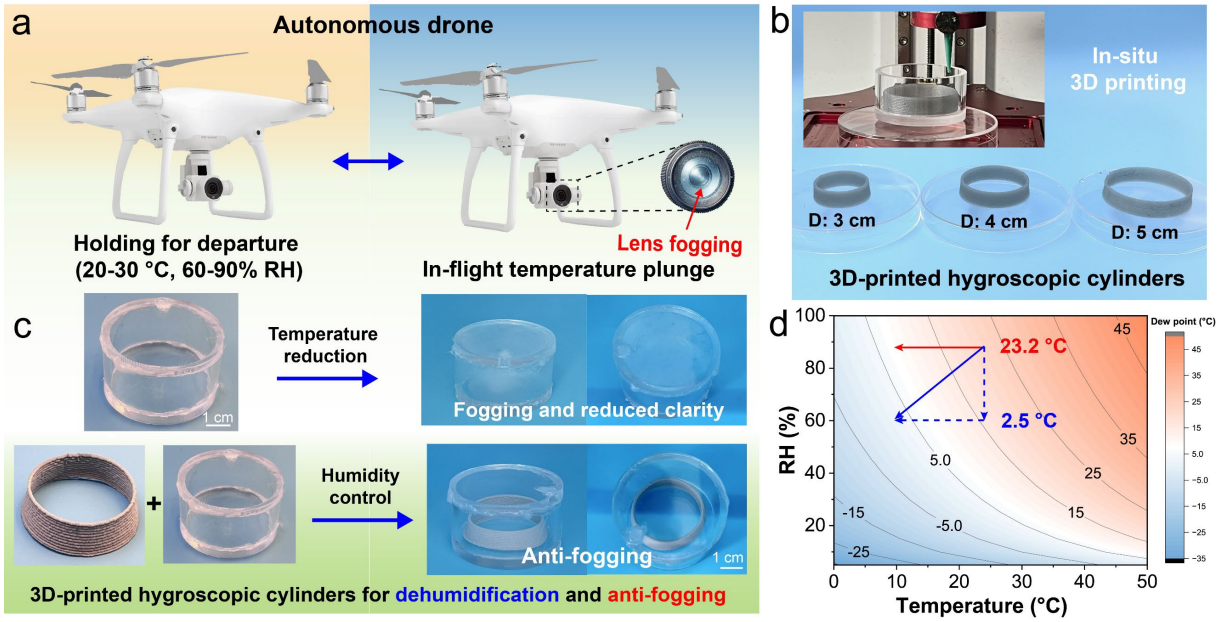

Figure 6. (a) Schematic illustration of autonomous drones subjected to temperature differential-induced camera fogging. (b) 3D-printed hygroscopic cylinders with varying dimensions. (c) Dehumidification testing for evaluating real-time fog prevention, and (d) isotherm contours of

dew point under varying temperatures and RH conditions.

Autonomous drones (unmanned aerial vehicles, UAVs) have become integral to diverse sectors including logistics, infrastructure inspection, environmental monitoring, defense and cinematography. The operational demands of UAVs necessitate reliable performance across frequent takeoff and landing cycles, particularly in complex terrains and under diverse climatic conditions.[69] One critical challenge arises from in-flight condensation induced by temperature differentials during takeoff and landing cycles (**Figure 6a**). Atmospheric moisture readily condensing on integrated circuits and optical surfaces — particularly lenses — reduces visibility, increases light scattering and compromises the reliability of computer vision systems. This challenge is further exacerbated in high-humidity environments, where moisture accumulation is more pronounced. While external condensation can be manually removed, internal condensation poses greater risks due to inaccessibility.

Sorption-based dehumidification operates via a water vapor separation mechanism and is inherently free from the temperature and humidity constraints that limit conventional refrigeration-based systems.[70] Consequently, sorption-based dehumidification offers a passive, energy-efficient solution particularly well-suited for enclosed environments, where traditional refrigeration-based dehumidifiers become energy-intensive or impractical. Emerging hygroscopic fabrics have shown potential for preventing fogging in automobile lamps and camera lenses,[71] while hygroscopic elastic foams have demonstrated promise as protective packaging materials for moisture-sensitive electronics.[27] However, device-level integration and experimental validation of defogging functionality remain unexplored. Beyond 3D-printed cubic matrices, this study expands the printing scope to include hygroscopic cylindrical structures using Ink-4, with diameters ranging from 3 to 5 cm (**Figure 6b** and Supporting Video S2). These hollow cylinders were specifically fabricated to evaluate their printability,

dehumidification and anti-fogging performance within the lens chambers of autonomous drones.

A four-faced transparent chamber (Inner diameter: 48 mm, volume: 36.2 mL) was constructed to emulate the environmental conditions within UAV lens compartments and subjected to rapid thermal cycling (**Figure 6c**). The chamber was initially set at ~93% RH at 25 °C to establish a consistent baseline for all measurements. Upon exposure to the temperature drop from 25 °C to 10 °C — mimicking UAV takeoff — fogging rapidly presented on the inner surfaces of this chamber within 2 min. In contrast, the integration of 0.5 g of pre-dried hollow hygroscopic cylinders entirely suppressed fog formation by effective moisture uptake, thereby retaining high transmittance (> 95%) of the transparent chamber.

To elucidate the defogging mechanism within the chamber, temporal RH profiles were recorded at varying temperatures (Figure S31, Supporting Information). At 25 °C, 15 °C and 5 °C, the RH values decreased to 60%, 64% and 75% within 30 min, respectively. In addition, **Figure 6d** presents the phase equilibrium boundaries of water vapor within the chamber, mapping dew point temperatures as a function of RH and ambient temperatures. At 25 °C and 90% RH, the dew point temperature was calculated to be 23.2 °C (Section S33, Supporting Information). Upon cooling the chamber to 10 °C — well below the dew point — water vapor rapidly condensed inside the chamber, leading to fog formation on interior surfaces. With the incorporation of a pre-dried hygroscopic cylinder, the internal RH value was reduced from 93% to 60%, corresponding to a dew point of 2.6 °C at 25 °C. Since the ambient temperature (10 °C) remained above this dew point, no water vapor condensation occurred, thereby preventing fog formation within the chamber. These results indicate the great potential of integrating hygroscopic cylinders to effectively reduce RH levels and to prevent fog formation within UAV lens compartments, thereby mitigating visibility loss during temperature and RH changes.

2.5 Broad applicability of granular hydrogel-mediated inks

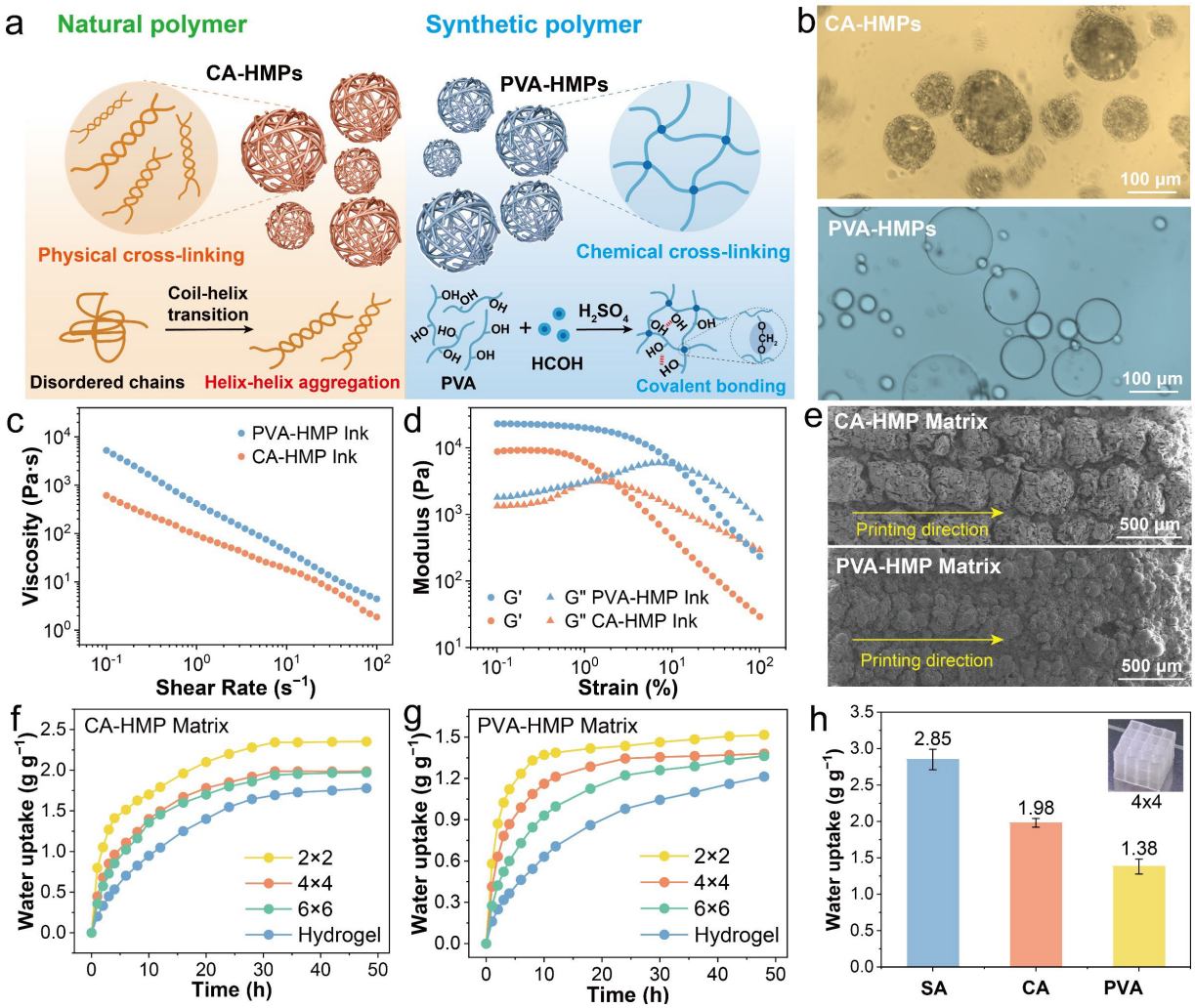

Figure 7. (a) chemical structures, cross-linking reactions and microsphere formation mechanism of κ-CA and PVA. (b) Optical microscope images of κ-CA and PVA HMPs. Rheological properties of different inks: (c) shear viscosities under shear rate sweep, and (d) G′ and G″ under oscillatory amplitude sweep. (e) SEM images of filament surfaces printed from CA-HMP and PVA-HMP inks. Water vapor sorption characterization of matrices based on (f) CA-HMP ink and (g) PVA-HMP ink. (h) Summary of water uptake capacity of three matrices after 48 h under 90% RH.

To evaluate the broad applicability of the microgel-mediated DIW method for printing hygroscopic 3D structures, additional bio-based and synthetic polymers were employed for the fabrication of HMPs and HMP inks. Different polymer microspheres can be synthesized by using physical or chemical methods.[72] The subsequent processes comprised cross-linking,

dual-network formation and centrifugation, which were identical to that used for SA-HMPs and SA-HMP inks. Chemical structures, cross-linking reactions and microgel formation mechanisms of new HMPs and HMP inks are illustrated in **Figure 7a**.

κ-Carrageenan (κ-CA) is a polysaccharide extracted from specific species of red algae, similar to SA.[73] The κ-CA backbone consists of alternating repeating units of 3,6-anhydrogalactose (3, 6-AG) and galactose-4-sulfate, connected via α-1, 3- and β-1, 4-glycosidic linkages. Notably, each disaccharide unit in κ-CA carries a sulfate group, endowing it with intrinsic hygroscopicity for AWH applications.[74] Neat κ-CA powder exhibits an equilibrium water uptake of ~0.68 g g^{-1} under 90% RH (Figure S32, Supporting Information). In addition, neat κ-CA is thermo-reversible and readily dissolves in warm water (~70 °C) due to electrostatic repulsion among polymer chains induced by the sulfate groups. To fabricate HMPs, κ-CA and surfactants were dissolved in water and emulsified with paraffin oil under vigorous vortexing, forming a water-in-oil suspension.[75] Upon cooling to room temperature, the characteristic sol−gel transition of κ-CA was triggered, yielding solid CA-HMPs (**Figure 7b**). In this process, the disordered polymer chains (initially present as random coils in warm solutions) reorganized into ordered double-helix conformations. Subsequent aggregation of neighboring helices led to the formation of heterotypic junction zones through helix−helix interactions within the polymer network.[75] The coil−to−helix transformation and helix−helix aggregation resulted in the gelation of CA-HMPs. Optical microscopy revealed that the CA-HMPs possessed an average particle size of 82.19 μm. (Figure S33a, Supporting Information). For dual-network formation, the negatively charged κ-CA exhibited salting-in effects with Li^+ ions, which formed electrostatic bridges between the sulfate groups and 3,6-anhydrogalactose (3,6-AG) moieties, yielding CA-HMP ink.

Polyvinyl alcohol (PVA) was employed as the synthetic polymer for fabricating HMPs. Neat PVA powder exhibits an equilibrium water uptake of ~0.15 g g^{-1} under 90% RH (Figure S32,

Supporting Information). Unlike the Ca^{2+}-induced ionic cross-linking in SA and temperature-responsive coil−helix transition in κ-CA, the PVA suspension in the water-in-oil system underwent covalent cross-linking through a reaction with formaldehyde under acidic conditions. This covalent network stabilized PVA-HMPs within the emulsion, enabling their subsequent separation and collection. PVA-HMPs exhibited an average particle size of 83.90 μm, as measured by optical microscopy (Figure S33b, Supporting Information).

Both CA-HMP and PVA-HMP inks exhibited pronounced shear thinning characteristics (**Figure 7c**). Oscillatory strain sweep revealed a transition from dominant elastic behavior (G′ > G″ at low strains) to a viscous-dominated response (G″ > G′ at high strains) (**Figure 7d**). Furthermore, dynamic recovery tests exhibited excellent reversibility between solid-like (G′ > G″ at 0.1% strain) and liquid-like (G″ > G′ at 100% strain) states across multiple cycles (Figure S34, Supporting Information). Consistent with the SA-HMP inks, these rheological results demonstrate their optimal printability for direct ink writing with high shape fidelity. SEM analysis confirmed the preservation of jammed HMPs within printed filaments for both inks (**Figure 7e**). Moreover, cyclic compression testing at 30% strain demonstrated exceptional mechanical stability in CA-HMP and PVA-HMP printed dense hydrogels (15 × 15 × 10 mm^3), exhibiting 9.2% and 4.8 % plastic deformation after 100 loading-unloading cycles (Figure S35 and S36 Supporting Information). These results highlight the structural integrity, durability and fatigue resistance of the printed hygroscopic materials based on CA-HMP and PVA-HMP inks.

Water vapor sorption was measured under 90% RH and at 25 °C. Three hygroscopic matrices with 2×2, 4×4 and 6×6 cuboid lattices (dimension: 15 × 15 × 10 mm^3) were printed from each ink, while a fully dense hydrogel with 100% infill was printed and characterized as a control group. For CA-HMP printed 3D structures, the water uptake of 2×2, 4×4 and 6×6 matrices after 48 h were 2.35, 1.98 and 1.97 g g^{-1}, respectively (**Figure 7f**). For PVA-HMP printed 3D structures, the corresponding water uptake values were 1.52, 1.38 and 1.36 g g^{-1}, respectively

(**Figure 7g**). Consistent with the SA-HMP printed 3D structures, the 2×2 matrix exhibited the highest water uptake capacity, while the fully dense hydrogel showed the lowest hygroscopic performance. To ensure reliable comparison, the water uptake values of 4×4 matrices printed from SA-, CA- and PVA-HMP inks are summarized in **Figure 7h**. For each matrix group, water uptake was measured from three independent samples. The SA-based matrix achieved the highest average water uptake of 2.85 g g^{-1} after 48 h, outperforming its CA- and PVA-based counterparts. This superior water uptake was primarily attributed to the pronounced swelling behavior of the SA-based filaments, which expanded by 1.6-fold in diameter — greater than the 1.39-fold and 1.35-fold increases observed in CA- and PVA-HMP-based filaments, respectively (Figure S37, Supporting Information). Furthermore, water desorption experiments were conducted on 4×4 matrices fabricated from SA-, CA- and PVA-HMP inks. All pre-dried matrices were first placed into a 90% RH chamber for 48 h, followed by dehydration in a hot-air oven at 80 °C. All three matrices exhibited rapid desorption kinetics, achieving near-complete moisture release within 2 h (Figure S38, Supporting Information). Notably, the SA-based matrix resulted in the fastest moisture release owing to its initially highest water uptake compared to other matrices. These results demonstrate the versatility of the microgel strategy in fabricating 3D hygroscopic structures, transforming a group of hygroscopic materials (e.g., biopolymers and synthetic polymers) into tailored 3D porous matrices for enhanced water vapor sorption and desorption.

3. Conclusions

In summary, a series of hygroscopic biopolymers (SA and κ-CA) and synthetic polymers (PVA) were transformed into micron-scale HMPs through distinct water−in−oil emulsion mechanisms. Jammed HMPs imparted sufficient viscosity and pronounced shear-thinning behavior to the inks, fulfilling the rheological requirements (viscosity, rheology and modulus) for aqueous DIW at ambient conditions. Embedding LiCl within HMPs enhanced moisture uptake, while

the introduction of additional percolating networks (i.e., P(PDMAPS-*co*-HEAA) and PAC) improved tensile and compressive strength, ensuring structural robustness of the printed matrix. The synergistic salt-in effect and the large-volume swelling of copolymer networks stabilized the LiCl within the matrices, minimizing LiCl leakage during cyclic moisture sorption/desorption. This microgel-based strategy significantly expands the range of hygroscopic materials compatible with 3D printing. Load-bearing 3D matrices with well-defined hierarchical structures were printed. This 3D lattice structure with hierarchical porosity — spanning millimeter-scale lattice channels, micrometer-scale wrinkled surfaces, and nanometer-scale HMP assemblies — maximized surface areas, and vapor and water transporting pathways enhancing sorption/desorption kinetics across a broad RH range. The hierarchical structures incorporated several performance-enhancing strategies that are rarely, if ever, simultaneously achieved in conventional hygroscopic aerogels, hydrogels, or foams. The optimized hygroscopic matrix (M2) reduced raw material requirement by 53% and increased specific surface areas by 5.8-fold, leading to 1.4-fold higher water uptake (2.85 g g^{-1} at 90% RH over 48 h) compared to the common hygroscopic aerogel (M4). The water uptake capability places M2 among the top-performing 3D-printed hygroscopic materials reported to date. Beyond 3D-printed cubic matrices, HMP inks expand the printing scope to fabricate hygroscopic cylindrical structures, enabling effective sorption-based dehumidification and anti-fogging performance within UAV lens compartments during temperature and RH changes. This study demonstrates the high precision, versatility and broad applicability of the microgel-mediated DIW method for 3D printing hygroscopic materials, establishing a new paradigm for designing hierarchically porous 3D matrices tailored for reliable moisture sorption/desorption and user-defined AWH applications.

4. Experimental section

4.1 Preparation of HMPs

SA-HMPs: SA-HMPs were fabricated by forming a water−in−oil (W/O) emulsion of sodium alginate aqueous solution, followed by ionic crosslinking with Ca^{2+} to solidify the emulsion droplets into microparticles. A sodium alginate aqueous solution (5 wt%, 10 mL) was emulsified in liquid paraffin (50 mL containing 2 wt% Span 20) under mechanical stirring at varying rotation speeds (200 − 800 rpm, 25 °C) for 1 h. Cross-linking was then performed by adding $CaCl_2$ solution (5 wt%, 1 mL) with continued stirring for 3 h. The resulting microparticles were collected by centrifugation at 7000 rpm for 3 min, followed by sequential washing with petroleum ether, ethanol and DI water to obtain SA-HMPs.

CA-HMPs: CA-HMPs were prepared via W/O emulsion and thermal gelation. A κ-carrageenan aqueous solution (5 wt%, 10 mL, 80 °C) was emulsified in liquid paraffin (50 mL containing 2 wt% Span 20) under mechanical stirring (1500 rpm, 80 °C) for 1 h. Gelation was achieved by cooling to room temperature. The resulting microparticles were collected by centrifugation at 7000 rpm for 3 min, followed by sequential washing with petroleum ether, ethanol and DI water to obtain CA-HMPs.

PVA-HMPs: PVA-HMPs were prepared via a W/O emulsion method with chemical crosslinking. A polyvinyl alcohol aqueous solution (10 wt%, 10 mL) containing H_2SO_4 (25 wt%, 0.4 mL) was emulsified in liquid paraffin (50 mL containing 2 wt% Span 20) under mechanical stirring (500 rpm, 50°C) for 30 min. Cross-linking was initiated by adding glutaraldehyde solution (10 wt%, 1 mL) and maintained at 50°C for 1 h. The resulting microparticles were collected by centrifugation at 7000 rpm for 3 min, followed by sequential washing with petroleum ether, ethanol and DI water to obtain PVA-HMPs.

4.2 Preparation of HMP inks

Each group of HMPs was mixed with the cross-linking solution at a fixed mass ratio of 1:2 (HMP: solution). The cross-linking solution was composed of 20 wt% DMAPS, 10 wt% HEAA, 0.5 wt% PAC, *α*-ketoglutaric acid (photoinitiator, 0.5 wt% relative to total monomer mass),

MBA (crosslinker, 1 wt% relative to total monomer mass) and LiCl (0.05 − 0.4 g mL^{-1}). The resulting mixture was collected by centrifugation at 5000 − 7000 rpm for 3 min to obtain HMP inks. At a fixed LiCl concentration of 0.1 mL^{-1}, the inks centrifuged at 5000, 6000 and 7000 rpm were labeled as Ink-1, Ink-2, and Ink-3, respectively. Under otherwise identical conditions, the ink formulation with an additional 0.5 wt% ATO was designated as Ink-4.

4.3 3D Printing

All matrices were designed using Materialise Magics software and exported as STL files. The 3D structures were subsequently imported into Repetier-Host software for slicing and conversion into 2D multi-layer planar data, generating G-code files. The G-code files were uploaded to the Allevi 2 bioprinter's on-premises system to configure printing parameters. For fabrication, the printing ink was loaded into a 10 mL syringe and extruded through a 0.5 mm diameter nozzle. The printing process was conducted with adjustable printing speeds (4 − 16 mm s^{-1}) and extrusion pressures (8 −10 psi). Following printing, the matrices were photocured under UV light (365 nm, 18 W) for 20 min, then sprayed with a 5 wt% $CaCl_2$ solution and cross-linked for 2 h, and finally freeze-drying for 24 h to obtain the aerogel matrices.

Declaration of competing interest

The authors declare no conflict of interest.

Acknowledgements

The authors acknowledge the financial support from the National Natural Science Foundation of China (Grant No. 22379133), Taishan Scholar Program of Shandong Province, China (Grant No. tsqn201812026), Natural Science Foundation of Shandong Province, China (Grant Nos. ZR2023MB087), Natural Science Foundation of Qingdao, China (Grant No. 23-2-1-243-zyyd-jch) and Fundamental Research Funds for the Central Universities, China (Grant No. 202561099).

References

[1] Y. Zhong, L. Zhang, X. Li, B. El Fil, C. D. Díaz-Marín, A. C. Li, X. Liu, A. LaPotin, E. N. Wang, *Nat. Rev. Mater.* **2024**, 9, 681.
[2] M. Wang, E. Liu, T. Jin, S.-u. Zafar, X. Mei, M.-L. Fauconnier, C. De Clerck, *Water Res.* **2024**, 250, 121052.
[3] W. Zeng, T. You, W. Wu, *Nano Energy* **2024**, 125, 109572.
[4] P. Poredoš, H. Shan, R. Wang, *Joule* **2022**, 6, 1390.
[5] R. Li, W. Wang, Y. Shi, C.-t. Wang, P. Wang, *Adv. Mater.* **2024**, 36, 2209460.
[6] J. Wang, L. Hua, C. Li, R. Wang, *Energy Environ. Sci.* **2022**, 15, 4867.
[7] Q. Luo, M. Chen, D. Yu, T. Zhang, J. Zhao, L. Zhang, X. Han, M. Zhou, Y. Hou, Y. Zheng, *ACS Nano* **2024**, 18, 14650.
[8] K. Yang, T. Pan, Q. Lei, X. Dong, Q. Cheng, Y. Han, *Environ. Sci. Technol.* **2021**, 55, 6542.
[9] S. Guo, Y. Zhang, S. C. Tan, *Device* **2023**, 1, 100099.
[10] W. Lu, W. L. Ong, G. W. Ho, *J. Mater. Chem. A* **2023**, 11, 12456.
[11] S. Bai, X. Yao, M. Y. Wong, Q. Xu, H. Li, K. Lin, Y. Zhou, T. C. Ho, A. Pan, J. Chen, Y. Zhu, S. Wang, C. Y. Tso, *ACS Nano* **2024**, 18, 31597.
[12] S. Gao, Y. Wang, C. Zhang, M. Jiang, S. Wang, Z. Wang, *Matter* **2023**, 6, 2182.
[13] J. Xu, P. Wang, Z. Bai, H. Cheng, R. Wang, L. Qu, T. Li, *Nat. Rev. Mater.* **2024**, 9, 722.
[14] T. Xu, X. Ding, H. Cheng, G. Han, L. Qu, *Adv. Mater.* **2024**, 36, 2209661.
[15] S. Guo, S. De Wolf, M. Sitti, C. Serre, S. C. Tan, *Adv. Mater.* **2024**, 36, 2311445.
[16] N. Hanikel, M. S. Prévot, O. M. Yaghi, *Nat. Nano.* **2020**, 15, 348.
[17] G. Tian, C. Fu, Z. Guo, *Mater. Today* **2025**, 83, 307.
[18] H. Shan, P. Poredoš, Z. Chen, X. Yang, Z. Ye, Z. Hu, R. Wang, S. C. Tan, *Nat. Rev. Mater.* **2024**, 9, 699.
[19] F. Ni, P. Xiao, C. Zhang, T. Chen, *Matter* **2022**, 5, 2624.
[20] H. Shan, P. Poredoš, H. Qu, X. Yang, M. Zhou, L. Bai, J. Shi, W. Chen, R. Wang, S. C. Tan, *Adv. Funct. Mater.* **2024**, 34, 2402839.
[21] Q. Li, F. Wang, Y. Zhang, M. Shi, Y. Zhang, H. Yu, S. Liu, J. Li, S. C. Tan, W. Chen, *Adv. Mater.* **2024**, 36, 2209479.
[22] Y. Song, M. Zeng, X. Wang, P. Shi, M. Fei, J. Zhu, *Adv. Mater.* **2024**, 36, 2209134.
[23] T. Li, T. Yan, P. Wang, J. Xu, X. Huo, Z. Bai, W. Shi, G. Yu, R. Wang, *Nat. Water* **2023**, 1, 971.
[24] W. Guan, Y. Zhao, C. Lei, G. Yu, *PNAS* **2023**, 120, e2308969120.
[25] S. Li, K. Shao, X. Wu, S. Wang, J. Li, C. Guo, L. Yu, P. Murto, X. Xu, *Adv. Funct. Mater.* **2024**, 34, 2310020.
[26] Y. Wang, S. Li, J. Li, Y. Sun, Z. Li, P. Murto, Z. Wang, X. Xu, *J. Mater. Chem. A* **2025**, 13, 4413.
[27] S. Li, R. Ou, J. Li, Z. Li, L. Yu, Z. Wang, P. Murto, X. Xu, *Chem. Eng. J.* **2025**, 516, 164217.
[28] Y. Zhao, W. Guan, Y. Z. Wong, C. Lei, Y. Wang, X. Liu, G. Yu, *PNAS* **2025**, 122, e2500928122.
[29] X. Du, Z. Xie, H. Zhang, S. Jiang, X. Su, J. Fan, *Adv. Mater.* **2025**, 37, 2505279.
[30] W. Guan, Y. Zhao, C. Lei, Y. Wang, K. Wu, G. Yu, *Adv. Mater.* **2025**, 37, 2420319.
[31] J. Li, C. Xu, L. Chen, X. Zhang, M. Zhu, Y. Cheng, *Adv. Funct. Mater.* **2025**, 35, 2423063.
[32] J. Lu, J. Yan, F. Pei, Z. Niu, J. Li, G. Han, D. Wang, Y. Yue, W. Cheng, *Adv. Funct. Mater.* **2025**, 35, 2505359.
[33] B. Lin, W. Ying, C. Li, J. Liu, L. Zhou, H. Zhang, R. Wang, J. Wang, *Adv. Funct. Mater.* **2025**, 35, 2500679.
[34] H. Zou, J. Zhu, X. Yang, Z. Zeng, D. Huang, J. Li, R. Wang, *Adv. Funct. Mater.* **2025**, 35, 2501163.
[35] Y. Yang, X. Zhou, X. Ji, W. Liu, Q. Li, C. Zhu, X. Li, S. Liu, X. Lu, J. Qu, *Adv. Funct.*

Mater. **2025**, 35, 2416776.
[36] Y. Lee, S. H. Nah, K.-Y. Wang, Y. Chi, J. B. Kim, Z. Zhang, S. Yang, *Adv. Funct. Mater.* **2025**, 35, 2506725.
[37] A. Ghaffarkhah, M. Panahi-Sarmad, S. Rostami, O. Zaremba, L. A. Bauman, S. A. Hashemi, S. Dutta, P. Yang, T. Guo, F. Jiang, S. Wuttke, M. Arjmand, O. J. Rojas, *Adv. Funct. Mater.* **2025**, 35, 2506427.
[38] Y. Hu, Y. Chen, J. Xu, W. Cheng, Y. Lu, G. Han, O. J. Rojas, *ACS Nano* **2025**, 19, 20881.
[39] J. Yang, J. Lu, D. Han, B. Zhou, A. Du, *Prog. Mater Sci.* **2025**, 152, 101462.
[40] X. Zhang, Y. Yan, N. Li, P. Yang, Y. Yang, G. Duan, X. Wang, Y. Xu, Y. Li, *Sci. Bull.* **2023**, 68, 203.
[41] S. Li, K. Shao, X. Wu, S. Wang, J. Li, C. Guo, L. Yu, P. Murto, X. Xu, *Adv. Funct. Mater.* **2024**, 34, 2310020.
[42] A. P. Dhand, M. D. Davidson, J. A. Burdick, *Nat. Rev. Bioeng.* **2025**, 3, 108.
[43] X. Zhang, J. Wang, X. Wang, Y. Xu, Y. Li, *Mater. Today* **2025**, 83, 484.
[44] Y. Chen, Z. Yu, Y. Ye, Y. Zhang, G. Li, F. Jiang, *ACS Nano* **2021**, 15, 1869.
[45] N. Li, K. Shao, J. He, S. Wang, S. Li, X. Wu, J. Li, C. Guo, L. Yu, P. Murto, J. Chen, X. Xu, *Small* **2023**, 19, 2301474.
[46] J. Gao, K. Shao, J. Li, N. Li, S. Wang, X. Wu, P. Murto, Z. Wang, Y. Zhou, X. Xu, *J. Mater. Chem. A* **2024**, 12, 6592.
[47] P. Zhu, Z. Yu, H. Sun, D. Zheng, Y. Zheng, Y. Qian, Y. Wei, J. Lee, S. Srebnik, W. Chen, G. Chen, F. Jiang, *Adv. Mater.* **2024**, 36, 2306653.
[48] Z. Chen, X. Yang, Q. Shao, R. Wang, *Adv. Funct. Mater.* **2025**, 35, 2508512.
[49] M. A. S. R. Saadi, A. Maguire, N. T. Pottackal, M. S. H. Thakur, M. M. Ikram, A. J. Hart, P. M. Ajayan, M. M. Rahman, *Adv. Mater.* **2022**, 34, 2108855.
[50] Z. Chen, D. Zhao, B. Liu, G. Nian, X. Li, J. Yin, S. Qu, W. Yang, *Adv. Funct. Mater.* **2019**, 29, 1900971.
[51] A. Feng, Y. Shi, C. Onggowarsito, X. S. Zhang, S. Mao, M. A. H. Johir, Q. Fu, L. D. Nghiem, *ChemSusChem* **2024**, 17, e202301905.
[52] X. Chang, S. Li, N. Li, S. Wang, J. Li, C. Guo, L. Yu, P. Murto, X. Xu, *J. Mater. Chem. A* **2022**, 10, 18170.
[53] C. B. Highley, K. H. Song, A. C. Daly, J. A. Burdick, *Adv. Sci.* **2019**, 6, 1801076.
[54] X. N. Zhang, Q. Zheng, Z. L. Wu, *Compos. Part B Eng.* **2022**, 238, 109895.
[55] A. C. Daly, L. Riley, T. Segura, J. A. Burdick, *Nat. Rev. Mater.* **2020**, 5, 20.
[56] Z. Chen, X. Wang, J. Liu, K. Liu, S. Li, M. Wu, Z. Wu, Z. Wang, Y. Shi, C. Ruan, *Adv. Funct. Mater.* **2025**, 35, 2417836.
[57] M. Wu, R. Li, Y. Shi, M. Altunkaya, S. Aleid, C. Zhang, W. Wang, P. Wang, *Mater. Horiz.* **2021**, 8, 1518.
[58] H. Zhang, Y. Cong, A. R. Osi, Y. Zhou, F. Huang, R. P. Zaccaria, J. Chen, R. Wang, J. Fu, *Adv. Funct. Mater.* **2020**, 30, 1910573.
[59] C. Cui, Z.-Y. Zhuang, H.-L. Gao, J. Pang, X.-F. Pan, S.-H. Yu, *Adv. Mater.* **2025**, 37, 2500782.
[60] F. Perin, E. Spessot, A. Famà, A. Bucciarelli, E. Callone, C. Mota, A. Motta, D. Maniglio, *ACS Biomater. Sci. Eng.* **2023**, 9, 1320.
[61] Q. Gao, X. Niu, L. Shao, L. Zhou, Z. Lin, A. Sun, J. Fu, Z. Chen, J. Hu, Y. Liu, Y. He, *Biofabrication* **2019**, 11, 035006.
[62] M. Hirsch, A. Charlet, E. Amstad, *Adv. Funct. Mater.* **2021**, 31, 2005929.
[63] R. Zhang, J. Guo, X. Yang, X. Jiang, L. Zhang, J. Zhou, X. Cao, B. Duan, *ACS Appl. Mater. Interfaces* **2023**, 15, 15917.
[64] X. Zhou, F. Zhao, Y. Guo, B. Rosenberger, G. Yu, *Sci. Adv.* **2019**, 5, eaaw5484.
[65] F. Li, N. Li, S. Wang, L. Qiao, L. Yu, P. Murto, X. Xu, *Adv. Funct. Mater.* **2021**, 31,

2104464.
[66] J. Sun, F. Ni, J. Gu, M. Si, D. Liu, C. Zhang, X. Shui, P. Xiao, T. Chen, *Adv. Mater.* **2024**, 36, 2314175.
[67] Z. Yang, M. Zhang, X. Zhao, Z. Guo, S. Zeb, W. Jiang, T. Liu, R. Hu, X. Jiang, *Chem. Eng. J.* **2024**, 479, 147442.
[68] S. Shi, N. Zhu, Y. Li, Y. Song, *Renew. Energy* **2024**, 235, 121178.
[69] S. Xu, R. Li, S. Tian, J. Yu, C. An, K. Yang, J. Yang, L. Zhang, *npj Flex Electron* **2025**, 9, 61.
[70] Y. Lin, K. Shao, S. Li, N. Li, S. Wang, X. Wu, C. Guo, L. Yu, P. Murto, X. Xu, *ACS Appl. Mater. Interfaces* **2023**, 15, 10084.
[71] Y. Zhang, L. Wu, A. A. Babar, X. Zhao, X. Wang, J. Yu, B. Ding, *Small Methods* **2021**, 5, 2101011.
[72] T. Guo, L. Luo, L. Wang, F. Zhang, Y. Liu, J. Leng, *ACS Nano* **2025**, 19, 18003.
[73] X. Lin, J. Wang, X. Wu, Y. Luo, Y. Wang, Y. Zhao, *Adv. Funct. Mater.* **2023**, 33, 2211323.
[74] J. He, N. Li, S. Wang, S. Li, C. Wang, L. Yu, P. Murto, X. Xu, *J. Mater. Chem. A* **2022**, 10, 8556.
[75] F. Bono, S. H. Strässle Zuniga, E. Amstad, *Adv. Funct. Mater.* **2025**, 35, 2413368.